Author(s): Hinkkanen, Marko & Awan, Hafiz & Qu, Zengcai & Tuovinen, Toni & Briz, Fernando

Title: Current Control for Synchronous Motor Drives: Direct Discrete-Time Pole-Placement Design

Year: 2015

Version: Post print

Please cite the original version:

Hinkkanen, Marko & Awan, Hafiz & Qu, Zengcai & Tuovinen, Toni & Briz, Fernando. 2015. Current Control for Synchronous Motor Drives: Direct Discrete-Time Pole-Placement Design. IEEE Transactions on Industry Applications. 12. ISSN 0093-9994 (printed). DOI: 10.1109/tia.2015.2495288.

Current Control for Synchronous Motor Drives: Direct Discrete-Time Pole-Placement Design

Marko Hinkkanen, *Senior Member, IEEE*, Hafiz Asad Ali Awan, Zengcai Qu, Toni Tuovinen, and Fernando Briz, *Senior Member, IEEE*

***Abstract*—This paper deals with discrete-time models and current control methods for synchronous motors with a magnetically salient rotor structure, such as interior permanent-magnet synchronous motors and synchronous reluctance motors (SyRMs). The dynamic performance of current controllers based on the continuous-time motor model is limited, particularly if the ratio of the sampling frequency to the fundamental frequency is low. An exact closed-form hold-equivalent discrete motor model is derived. The zero-order hold of the stator-voltage input is modeled in stationary coordinates, where it physically is. An analytical discrete-time pole-placement design method for two-degrees-of-freedom proportional–integral current control is proposed. The proposed method is easy to apply: only the desired closed-loop bandwidth and the three motor parameters ($R_\mathrm{s}, L_\mathrm{d}, L_\mathrm{q}$) are required. The robustness of the proposed current control design against parameter errors is analyzed. The controller is experimentally verified using a 6.7-kW SyRM drive.**

***Index Terms*—Current control, delay, discrete-time model, interior permanent-magnet synchronous motor (IPM), saliency, synchronous reluctance motor (SyRM), zero-order hold (ZOH).**

I. Introduction

SYNCHRONOUS motors with a magnetically salient rotor—such as interior permanent-magnet synchronous motors (IPMs), synchronous reluctance motors (SyRMs), and permanent-magnet (PM)-assisted SyRMs—are more and more applied in hybrid (or electric) vehicles, heavy-duty working machines, and industrial applications. In these applications, the maximum speeds and, consequently, the maximum operating frequencies can be very high (e.g., 12 000 r/min corresponding to the frequency of 1000 Hz for a ten-pole machine). Since the switching frequency of the converter feeding the motor is limited due to the losses, the resulting ratio between the switching frequency and the maximum fundamental frequency can be even below 10. This will affect the sampling frequency, too, as it is typically either equal to the switching frequency or twice the switching frequency.

Generally, the stator current of synchronous motor drives is controlled in rotor coordinates [1]–[13]. This coordinate system is a natural selection since the controllable quantities are dc in steady state, the inductance matrix and the PM flux vector are (ideally) constant, and other parts of the control system typically operate in rotor coordinates. The most widely used approach is a synchronous-frame proportional–integral (PI) controller, often augmented with decoupling terms to compensate for the cross coupling due to the rotating coordinate system [1]–[6]. Disturbance rejection can be further improved with additional feedback from the stator current, referred to as an active resistance [4], [8], [11], [14]. Most of these two-degrees-of-freedom (2DOF) PI current controllers can be also represented as full-state feedback controllers with integral action and reference feedforward; this framework simplifies the systematic design and analysis of controllers.

Surface permanent-magnet synchronous motors (SPMs) and other magnetically nonsalient motors can be conveniently modeled using complex space vectors [3]–[6], [9], [14], [15]. From a current controller perspective, a plant to be controlled is the stator admittance, which can be represented as a complex transfer function [16]. The closed-loop poles can be placed in the desired locations, and the predetermined response is ideally achieved. On the other hand, in the case of IPMs and other salient motors, real space vectors (or the dq components) are needed. The stator admittance becomes a 2×2 transfer function matrix, which impedes the controller design procedure, since pole placement of multiple-input–multiple-output (MIMO) systems is not generally unique [17]. Furthermore, generalizing the current control designs of SPM drives to suit IPM drives is not trivial; sometimes, rough approximations are used [6], [13], or a generalization method is not explained [9].

A current controller can be first designed in the continuous-time domain and then discretized for the digital implementation using, e.g., the Euler or Tustin approximation [1], [3]–[6], [15]. This approach is well understood and works well in most applications. However, the ratio between the sampling frequency and the maximum operating frequency should be more than 15 in the case of an SPM [9], whereas IPMs and SyRMs are known to be even more demanding from this perspective [10], [13]. Similarly, the closed-loop control bandwidth is also limited by the sampling frequency. Higher maximum speeds, higher

Manuscript received April 8, 2015; revised August 5, 2015; accepted October 21, 2015. Paper 2015-IDC-0212.R1, presented at the 2015 IEEE Workshop on Electrical Machines Design, Control and Diagnosis, Turin, Italy, March 26–27, and approved for publication in the IEEE TRANSACTIONS ON INDUSTRY APPLICATIONS by the Industrial Drives Committee of the IEEE Industry Applications Society. This work was supported in part by ABB Oy and in part by the Academy of Finland.

M. Hinkkanen and H. Asad Ali Awan are with the Department of Electrical Engineering and Automation, Aalto University, 02150 Espoo, Finland (e-mail: marko.hinkkanen@aalto.fi; hafiz.awan@aalto.fi).

Z. Qu and T. Tuovinen are with ABB Oy Drives, 00380 Helsinki, Finland (e-mail: eric.qu@fi.abb.com; toni.tuovinen@alumni.helsinki.fi).

F. Briz is with the Department of Electrical, Electronic, Computer and Systems Engineering, University of Oviedo, 33204 Gijón, Spain (e-mail: fernando@isa.uniovi.es).

Color versions of one or more of the figures in this paper are available online at http://ieeexplore.ieee.org.

Digital Object Identifier 10.1109/TIA.2015.2495288

dynamic performance, and better robustness at a given sampling frequency could be achieved by designing the controller directly in the discrete-time domain [2], [7], [9], [10], [12], [13].

A hold-equivalent discrete model—including the effects of the zero-order hold (ZOH) and a sampler—of the motor drive is needed for the direct discrete-time control design. The exact closed-form hold-equivalent models have been derived for induction motor drives in [18] and for SPM drives in [7] and [9]. An approximate discrete model of IPM drives has been proposed in [10] and [12], but the exact closed-form expressions valid for IPM drives are not available in the literature.

Furthermore, a computational delay (an actuator delay) of one sampling period typically exists in the control loop. In the continuous-time domain, this delay can be approximated as a first-order low-pass filter and compensated for in the controller [15]. In the discrete-time domain, the delay can be modeled in an exact manner easily [7], [9], [10], [12]. If the state-feedback controller were used, the controller output could be stored in the memory, and the delayed output could be then used as an additional state in the state feedback law [19]. This simple approach is well known in control theory, but it has not been applied to discrete-time current control.

A few direct discrete-time current controller designs for IPMs are available [7], [10], [12], [13]. The controller proposed in [7] is based on the exact (but numerically evaluated) hold-equivalent discrete-time model, and the computational delay is taken into account. However, the controller is complicated, and its order is unnecessarily high. The methods in [10], [12], and [13] are based on approximations, which makes it difficult to evaluate their performance. Pole-placement designs, enabling simple analytic controller tuning, are not available for IPM drives.

In this paper, current control designs suitable for IPM drives are considered. First, the IPM model in the continuous-time domain is reviewed in Section II. Then, the main results are presented as follows.

1) Continuous-time 2DOF PI current controller designs for SPM drives [3], [4], [14] are extended to IPM drives in Section III. A basis for the generalization is that 2×2 coefficient matrices of the transfer function matrix are analogous to complex coefficients of the complex transfer function; this approach is kin to block-pole placement of MIMO systems [20], [21]. State control with integral action and reference feedforward is used as a design framework.
2) An exact closed-form hold-equivalent discrete model for IPM drives is presented in Section IV and derived in Appendix A. The ZOH of the stator-voltage input is modeled in stationary coordinates, where it physically is. The model can be applied to the design, analysis, and implementation of controllers and observers (e.g., in connection with deadbeat [22] or predictive [23] direct torque control methods).
3) An analytical direct discrete-time design method for a 2DOF PI current controller is proposed in Section V. The method is analogous to its continuous-time counterpart discussed in Section III, but it is based on the discrete-time model, and the computational delay is taken into account in the state feedback law. The proposed method is easy to apply: only the desired closed-loop bandwidth and the three motor parameters are needed.

The robustness of the proposed current control design against parameter errors is analyzed in Section VI. The operation of the controller is further investigated by means of simulations and experiments using a 6.7-kW SyRM drive. Naturally, the model and the control design method are directly applicable to SPM drives as well.

II. Continuous-Time Modeling

In order to model IPMs, real space vectors will be used throughout this paper. For example, the stator-current vector is $\boldsymbol{i}_s = [i_d, i_q]^T$, where i_d and i_q are the components of the vector, and the matrix transpose is marked with the superscript T. The identity matrix, the orthogonal rotation matrix, and the zero matrix are respectively defined as[1]

$$\mathbf{I} = \begin{bmatrix} 1 & 0 \\ 0 & 1 \end{bmatrix} \quad \mathbf{J} = \begin{bmatrix} 0 & -1 \\ 1 & 0 \end{bmatrix} \quad \mathbf{O} = \begin{bmatrix} 0 & 0 \\ 0 & 0 \end{bmatrix}. \tag{1}$$

Vectors are denoted using boldface lowercase letters, and matrices are denoted using boldface uppercase letters. Space vectors in stator coordinates are marked with the superscript s; no superscript is used for space vectors in rotor coordinates. The time dependence of the variables is denoted by the argument t.

The standard model of the IPM in rotor coordinates is considered. The electrical angle of the rotor is denoted by ϑ_m, and the electrical angular speed is

$$\frac{d\vartheta_m(t)}{dt} = \omega_m. \tag{2}$$

When the stator-current vector is chosen as a state variable, the state equation becomes

$$\frac{d\boldsymbol{i}_s(t)}{dt} = \boldsymbol{F}_c \boldsymbol{i}_s(t) + \boldsymbol{G}_c \boldsymbol{u}_s(t) + \boldsymbol{g}_c \psi_f \tag{3}$$

where the inputs are the stator-voltage vector $\boldsymbol{u}_s$ and the PM flux ψ_f (which is constant). The system matrices are

$$\boldsymbol{F}_c = \begin{bmatrix} -R_s/L_d & \omega_m L_q/L_d \\ -\omega_m L_d/L_q & -R_s/L_q \end{bmatrix}$$
$$\boldsymbol{G}_c = \begin{bmatrix} \frac{1}{L_d} & 0 \\ 0 & \frac{1}{L_q} \end{bmatrix} \quad \boldsymbol{g}_c = \begin{bmatrix} 0 \\ -\omega_m/L_q \end{bmatrix} \tag{4}$$

where R_s is the stator resistance, L_d is the direct-axis inductance, L_q is the quadrature-axis inductance, and the subscript c refers to the continuous-time model. If $L_d = L_q$, the model represents the SPM. If $\psi_f = 0$, the model of the SyRM is obtained.

[1]The notation is very similar to that obtained for complex space vectors: the rotation matrix $\mathbf{J}$ corresponds to the imaginary unit j, and the coordinate transformation matrices can be expressed using matrix exponentials, i.e., $e^{\vartheta \mathbf{J}} = \cos\vartheta \mathbf{I} + \sin\vartheta \mathbf{J}$.

The model can be expressed in the Laplace domain as

$$\boldsymbol{i}_s(s) = \boldsymbol{Y}_c(s)\left[\boldsymbol{u}_s(s) - \boldsymbol{u}_i(s)\right] \tag{5}$$

where the transfer function matrix is

$$\boldsymbol{Y}_c(s) = (s\mathbf{I} - \boldsymbol{F}_c)^{-1}\boldsymbol{G}_c = \begin{bmatrix} R_s + sL_d & -\omega_m L_q \\ \omega_m L_d & R_s + sL_q \end{bmatrix}^{-1} \tag{6}$$

and $\boldsymbol{u}_i = [0, \omega_m \psi_f]^T$ is the voltage induced by the PM flux. This induced voltage can be considered as a load disturbance from the current controller point of view.

III. Continuous-Time Current Control Design

A. Framework

For starters, a 2DOF PI current controller is reviewed in the continuous-time domain. A state controller with integral action and reference feedforward will be used as a design framework. In the Laplace domain, this control law, expressed in rotor coordinates, is

$$\boldsymbol{u}_{s,\mathrm{ref}}(s) = \boldsymbol{K}_{\mathrm{tc}}\boldsymbol{i}_{s,\mathrm{ref}}(s) + \frac{\boldsymbol{K}_{\mathrm{ic}}}{s}\left[\boldsymbol{i}_{s,\mathrm{ref}}(s) - \boldsymbol{i}_s(s)\right] - \boldsymbol{K}_{1c}\boldsymbol{i}_s(s) \tag{7}$$

where $\boldsymbol{u}_{s,\mathrm{ref}}$ is the resulting reference voltage, $\boldsymbol{i}_{s,\mathrm{ref}}$ is the reference current, $\boldsymbol{K}_{\mathrm{tc}}$ is the feedforward gain, $\boldsymbol{K}_{\mathrm{ic}}$ is the integral gain, and $\boldsymbol{K}_{1c}$ is the state-feedback gain. The gains are real 2×2 matrices. The voltage production of the inverter is assumed to be accurate and delayless, i.e., $\boldsymbol{u}_s = \boldsymbol{u}_{s,\mathrm{ref}}$ holds.

Integral action of the controller compensates for the PM-induced voltage $\boldsymbol{u}_i$, which is ideally a quasi-constant vector in dq coordinates. However, harmonics in PM-flux linkage distribution may cause a steady-state current ripple, which could be reduced by augmenting the controller (7) with a feedforward compensation method [2].

B. Block-Pole Placement

Using (5) and (7), the closed-loop current response becomes

$$\boldsymbol{i}_s(s) = \boldsymbol{H}_c(s)\boldsymbol{i}_{s,\mathrm{ref}}(s) - \boldsymbol{Y}_{\mathrm{ic}}(s)\boldsymbol{u}_i(s). \tag{8}$$

The closed-loop transfer function matrices are

$$\boldsymbol{H}_c(s) = \left(s^2\mathbf{I} + s\boldsymbol{A}_{1c} + \boldsymbol{A}_{0c}\right)^{-1}\left(s\boldsymbol{B}_{1c} + \boldsymbol{B}_{0c}\right) \tag{9}$$

$$\boldsymbol{Y}_{\mathrm{ic}}(s) = \left(s^2\mathbf{I} + s\boldsymbol{A}_{1c} + \boldsymbol{A}_{0c}\right)^{-1}\left(s\boldsymbol{G}_c\right) \tag{10}$$

where the 2×2 coefficient matrices are

$$\begin{aligned} \boldsymbol{A}_{0c} &= \boldsymbol{G}_c\boldsymbol{K}_{\mathrm{ic}} \quad \boldsymbol{A}_{1c} = \boldsymbol{G}_c\boldsymbol{K}_{1c} - \boldsymbol{F}_c \\ \boldsymbol{B}_{0c} &= \boldsymbol{G}_c\boldsymbol{K}_{\mathrm{ic}} \quad \boldsymbol{B}_{1c} = \boldsymbol{G}_c\boldsymbol{K}_{\mathrm{tc}}. \end{aligned} \tag{11}$$

It is worth noticing that $\boldsymbol{B}_{0c} = \boldsymbol{A}_{0c}$, which naturally agrees with the obvious steady-state condition $\boldsymbol{H}_c(0) = \mathbf{I}$ caused by integral action of the controller (7).

The coefficient matrices in (11) can be considered as extensions of complex (scalar) coefficients of the complex transfer functions, applied in modeling of SPMs. The coefficient matrices define the system poles, which are the zeros of $\det(s^2\mathbf{I} + s\boldsymbol{A}_{1c} + \boldsymbol{A}_{0c})$. The gain matrices can be solved from (11) as

$$\begin{aligned} \boldsymbol{K}_{\mathrm{tc}} &= \hat{\boldsymbol{G}}_c^{-1}\boldsymbol{B}_{1c\star} \quad \boldsymbol{K}_{\mathrm{ic}} = \hat{\boldsymbol{G}}_c^{-1}\boldsymbol{A}_{0c\star} \\ \boldsymbol{K}_{1c} &= \hat{\boldsymbol{G}}_c^{-1}(\hat{\boldsymbol{F}}_c + \boldsymbol{A}_{1c\star}) \end{aligned} \tag{12}$$

where the desired coefficient matrices are marked with the subscript $\star$, and the hat indicates parameter estimates. The poles and transmission zeros of (9) can be placed arbitrarily via the coefficient matrices using (12). The gains depend on the rotor speed via the matrices $\hat{\boldsymbol{F}}_c$ and $\hat{\boldsymbol{G}}_c$.

C. Selection of Coefficient Matrices

General reference tracking objectives for current controllers are as follows: 1) no cross coupling between the d- and q-axes and 2) the same closed-loop dynamics for both axes. Hence, the nondiagonal elements of $\boldsymbol{H}_c(s)$ should be zero due to the first objective, and the diagonal elements should be equal due to the second objective. In the following, two current controllers designed for SPM drives will be extended to IPM drives.

1) Internal Model Control Design: Choosing the coefficient matrices

$$\boldsymbol{A}_{0c\star} = \alpha^2\mathbf{I} \quad \boldsymbol{A}_{1c\star} = 2\alpha\mathbf{I} \quad \boldsymbol{B}_{1c\star} = \alpha\mathbf{I} \tag{13}$$

leads to the desirable closed-loop transfer function matrix

$$\boldsymbol{H}_{c\star}(s) = \frac{\alpha}{s + \alpha}\mathbf{I} \tag{14}$$

which corresponds to the first-order unity-gain low-pass filter having the bandwidth of α. If accurate parameter estimates in (12) are assumed, $\boldsymbol{H}_c(s) = \boldsymbol{H}_{c\star}(s)$ holds. Furthermore, closed-loop disturbance rejection (10) reduces to the diagonal transfer function matrix

$$\boldsymbol{Y}_{\mathrm{ic}\star}(s) = \frac{s}{(s + \alpha)^2}\hat{\boldsymbol{G}}_c. \tag{15}$$

This design may need a significant control effort at higher speeds, where the open-loop dynamics in (6) have large nondiagonal elements (i.e., strong cross coupling between the axes).

It can be shown that the controller consisting of (7), (12), and (13) is equal to the so-called internal model controller considered in [3], [11], and [24]. The advantages of this approach are its simplicity and easy tuning: only the desired bandwidth α and three parameter estimates ($\hat{R}_s$, $\hat{L}_d$, and $\hat{L}_q$) are needed.

2) Complex Vector Design: Choosing the coefficient matrices

$$\boldsymbol{A}_{0c\star} = \alpha\mathbf{I}(\alpha\mathbf{I} - \hat{\boldsymbol{F}}_c) \quad \boldsymbol{A}_{1c\star} = 2\alpha\mathbf{I} - \hat{\boldsymbol{F}}_c \quad \boldsymbol{B}_{1c\star} = \alpha\mathbf{I} \tag{16}$$

leads to same desirable reference tracking (14). On the other hand, disturbance rejection is governed by

$$\boldsymbol{Y}_{\mathrm{ic}\star}(s) = \frac{s}{s + \alpha}\left[(s + \alpha)\mathbf{I} - \hat{\boldsymbol{F}}_c\right]^{-1}\hat{\boldsymbol{G}}_c \tag{17}$$

where the nondiagonal elements of the open-loop dynamics (6) are preserved, thus reducing the control effort and improving

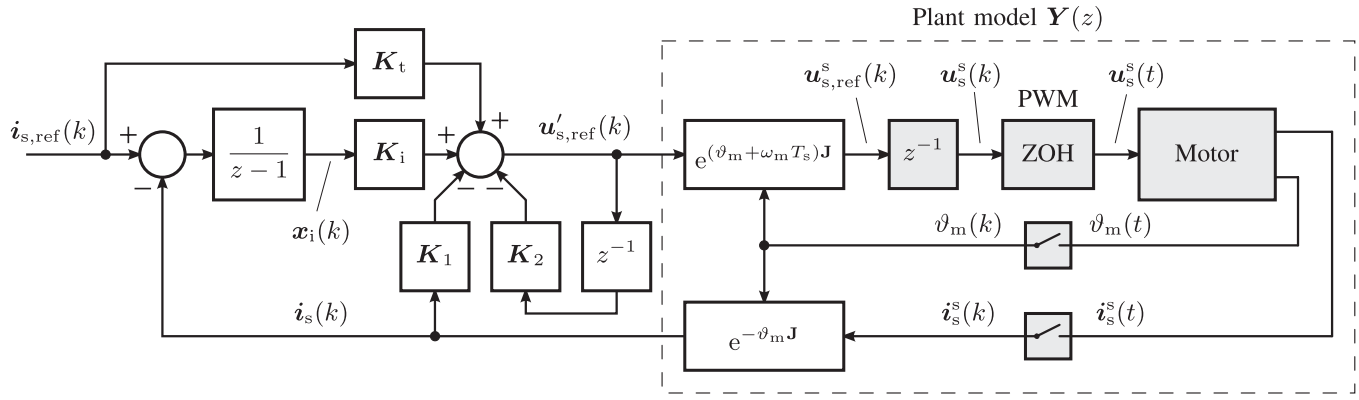

Fig. 1. State-feedback current controller with integral action and reference feedforward. The gray blocks represent the physical system (including the motor, PWM, samplers, and inherent computational delay z^{-1}). The block "Motor" consists of (2), (3), and the coordinate transformations. The PWM is modeled as the ZOH in stator coordinates. The sampling of the stator currents is synchronized with the PWM. The white blocks represent the discrete-time control algorithm. The angular error due to the time delay is compensated for in the coordinate transformation of the stator voltage.

robustness at higher speeds. The design (16) can be seen as an extension of the complex vector design [4] to IPMs.[2]

D. Digital Implementation

For digital implementation, continuous-time control algorithms have to be discretized using, e.g., the Euler or Tustin methods. Unfortunately, unless the sampling frequency is much higher than the closed-loop bandwidth and the maximum operating frequency, the actual closed-loop system deviates significantly from (14) due to discretization errors, leading to the cross coupling between the d- and q-axes, oscillations, or even instability [8], [9]. The performance of continuous-time designs is acceptable if the sampling frequency is about 20 times higher than the closed-loop bandwidth and the operating frequency. At lower sampling frequencies, direct discrete-time design methods are preferred.

IV. Discrete-Time Modeling

A. Closed-Form Hold-Equivalent Exact Model

Fig. 1 represents the current-controlled motor drive as a sampled data system, which consists of the continuous-time motor model, discrete-time controller, pulsewidth modulator (PWM), and samplers. Sampling is assumed to be synchronized with the PWM. The switching cycle averaged quantities are considered. Hence, the actual stator voltage $\boldsymbol{u}^s_s(t)$ in stator coordinates is piecewise constant between two consecutive sampling instants, which corresponds to the ZOH in stator coordinates.

A ZOH-equivalent discrete motor model is needed for the direct discrete-time control design. At this point, the system without the computational time delay is considered, i.e., only the effects of the ZOH and sampling are taken into account. The system model will be then augmented with the time delay of one sampling period T_s in Section IV-C. The discrete-time IPM model in rotor coordinates can be expressed as

$$\boldsymbol{i}_s(k+1) = \boldsymbol{F}\boldsymbol{i}_s(k) + \boldsymbol{G}\boldsymbol{u}_s(k) + \boldsymbol{g}\psi_f \tag{18}$$

[2]In [4], the resistance estimate $\hat{R}_s = 0$ was assumed for $\hat{\boldsymbol{F}}_c$ in (16).

where $\boldsymbol{F}$, $\boldsymbol{G}$, and $\boldsymbol{g}$ are the system matrices, and k is the discrete-time index. The exact closed-form expressions for these matrices are derived in Appendix A. To reduce the computation time, the trigonometric and hyperbolic functions needed in these expressions can be implemented with lookup tables.

B. Approximation Based on Series Expansion

The exact system matrix $\boldsymbol{F}$ can be also expressed using the series expansion [19]

$$\boldsymbol{F} = \mathbf{I} + T_s\,\boldsymbol{\Psi}\boldsymbol{F}_c \tag{19}$$

where

$$\boldsymbol{\Psi} = \mathbf{I} + \frac{T_s\boldsymbol{F}_c}{2!} + \frac{T_s^2\boldsymbol{F}_c^2}{3!} + \cdots. \tag{20}$$

Since the PM flux is constant in rotor coordinates, the input matrix for the PM flux is $\boldsymbol{g} = T_s\,\boldsymbol{\Psi}\boldsymbol{g}_c$.

The exact input matrix $\boldsymbol{G}$ cannot be easily expressed as a series expansion. If the ZOH of the stator voltage were in rotor coordinates, the matrix $\boldsymbol{G}$ would be equal to $T_s\,\boldsymbol{\Psi}\boldsymbol{G}_c$. However, the voltage is kept constant in stator coordinates during the sampling period, as discussed before. In [25], an approximate compensation for this effect was derived. Applying this compensation, the input matrix for the voltage can be approximated as

$$\boldsymbol{G} \approx T_s\,\boldsymbol{\Psi}\boldsymbol{G}_c \frac{\frac{\omega_m T_s}{2}}{\sin\left(\frac{\omega_m T_s}{2}\right)} e^{-\left(\frac{\omega_m T_s}{2}\right)\mathbf{J}}. \tag{21}$$

Typically, the first two terms of (20) suffice, i.e., $\boldsymbol{\Psi} = \mathbf{I} + (T_s/2)\boldsymbol{F}_c$. This model requires less memory but longer computation time compared with the exact model implemented with lookup tables. Choosing $\boldsymbol{\Psi} = \mathbf{I}$ yields the Euler approximation, which is computationally efficient but leads to much larger approximation errors.

C. Inclusion of the Control Delay

Fig. 1 shows the plant model from the control system point of view. As shown in the figure, the digital control system and

PWM update have (at least) one-sampling-period time delay due to the finite computation time, i.e., $\boldsymbol{u}_s^s(k) = \boldsymbol{u}_{s,\mathrm{ref}}^s(k-1)$ in stator coordinates, or, when transformed into rotor coordinates, $\boldsymbol{u}_s(k) = e^{-\omega_m T_s \mathbf{J}} \boldsymbol{u}_{s,\mathrm{ref}}(k-1)$. To simplify the notation, $\boldsymbol{u}'_{s,\mathrm{ref}} = e^{-\omega_m T_s \mathbf{J}} \boldsymbol{u}_{s,\mathrm{ref}}$ is defined, giving $\boldsymbol{u}_s(k) = \boldsymbol{u}'_{s,\mathrm{ref}}(k-1)$. The effect of the delay on the voltage angle can be easily compensated for in the coordinate transformation of the reference voltage (see Fig. 1).

For control design, the time delay can be included in the plant model as [19]

$$\begin{bmatrix} \boldsymbol{i}_s(k+1) \\ \boldsymbol{u}_s(k+1) \end{bmatrix} = \begin{bmatrix} \boldsymbol{F} & \boldsymbol{G} \\ \mathbf{O} & \mathbf{O} \end{bmatrix} \begin{bmatrix} \boldsymbol{i}_s(k) \\ \boldsymbol{u}_s(k) \end{bmatrix} + \begin{bmatrix} \mathbf{O} \\ \mathbf{I} \end{bmatrix} \boldsymbol{u}'_{s,\mathrm{ref}}(k) + \begin{bmatrix} \boldsymbol{g} \\ \mathbf{0} \end{bmatrix} \psi_f. \tag{22}$$

Both states are readily available as feedback signals in the state-feedback control: $\boldsymbol{i}_s$ is the measured feedback, and $\boldsymbol{u}_s$ is obtained from the previous value of the reference voltage $\boldsymbol{u}'_{s,\mathrm{ref}}$.

In the following section, the current controller will be designed based on the reference-tracking characteristics (similarly as in Section III). The disturbance-rejection characteristics are determined by the same system poles, which will be placed by the state feedback. Hence, the transfer function matrix from the disturbance voltage $\boldsymbol{u}_i$ to the stator current can be dropped from the following equations without loss of generality (and if needed, it can be taken into account separately based on the superposition principle). From (22), the stator current in the z-domain can be expressed as $\boldsymbol{i}_s(z) = \boldsymbol{Y}(z)\boldsymbol{u}'_{s,\mathrm{ref}}(z)$, where

$$\boldsymbol{Y}(z) = z^{-1}(z\mathbf{I} - \boldsymbol{F})^{-1}\boldsymbol{G}. \tag{23}$$

V. Discrete-Time Current Control Design

A. Framework

A state-feedback controller with integral action and reference feedforward, shown in Fig. 1, is considered. The control law is

$$\boldsymbol{x}_i(k+1) = \boldsymbol{x}_i(k) + \boldsymbol{i}_{s,\mathrm{ref}}(k) - \boldsymbol{i}_s(k) \tag{24a}$$

$$\boldsymbol{u}'_{s,\mathrm{ref}}(k) = \boldsymbol{K}_t \boldsymbol{i}_{s,\mathrm{ref}}(k) + \boldsymbol{K}_i \boldsymbol{x}_i(k) - \boldsymbol{K}_1 \boldsymbol{i}_s(k) - \boldsymbol{K}_2 \boldsymbol{u}_s(k) \tag{24b}$$

where $\boldsymbol{x}_i$ is the integral state, $\boldsymbol{K}_i$ is the integral gain, $\boldsymbol{K}_t$ is the feedforward gain, $\boldsymbol{K}_1$ and $\boldsymbol{K}_2$ are the state-feedback gains, and $\boldsymbol{u}_s(k+1) = \boldsymbol{u}'_{s,\mathrm{ref}}(k)$. Since all the states are directly available, the closed-loop poles can be placed arbitrarily. The control law (24) can be expressed in the z-domain as

$$\boldsymbol{u}'_{s,\mathrm{ref}}(z) = \boldsymbol{K}_t \boldsymbol{i}_{s,\mathrm{ref}}(z) + \frac{\boldsymbol{K}_i}{z-1}\left[\boldsymbol{i}_{s,\mathrm{ref}}(z) - \boldsymbol{i}_s(z)\right] - \boldsymbol{K}_1 \boldsymbol{i}_s(z) - \frac{\boldsymbol{K}_2}{z}\boldsymbol{u}'_{s,\mathrm{ref}}(z). \tag{25}$$

If needed, the control law can be augmented with a feedforward compensation method for nonsinusoidal PM-flux distribution [2].

B. Approximation of the Continuous-Time Design

The gains of the discrete-time controller (24) can be determined by approximating the continuous-time controller (see Section III) with the Euler method. In the framework of Fig. 1, the angular error of $\omega_m T_s$ due to the computational delay is compensated for in the coordinate transformation. When approximating continuous-time designs, the angular error of $\omega_m T_s/2$ caused by the ZOH delay should be also taken into account [25]. Embedding this compensation into the gains yields

$$\begin{aligned} \boldsymbol{K}_1 &= e^{\left(\frac{\omega_m T_s}{2}\right)\mathbf{J}} \boldsymbol{K}_{1c} \quad \boldsymbol{K}_2 = \mathbf{O} \\ \boldsymbol{K}_t &= e^{\left(\frac{\omega_m T_s}{2}\right)\mathbf{J}} \boldsymbol{K}_{\mathrm{tc}} \quad \boldsymbol{K}_i = T_s e^{\left(\frac{\omega_m T_s}{2}\right)\mathbf{J}} \boldsymbol{K}_{\mathrm{ic}} \end{aligned} \tag{26}$$

where the continuous-time gains $\boldsymbol{K}_{1c}$, $\boldsymbol{K}_{\mathrm{tc}}$, and $\boldsymbol{K}_{1c}$ are obtained using (12) with either (13) for the internal model control design or (16) for the complex vector design.

C. Proposed Block-Pole Placement

From (23) and (25), the closed-loop dynamics become

$$\boldsymbol{i}_s(z) = \boldsymbol{H}(z)\boldsymbol{i}_{s,\mathrm{ref}}(z) \tag{27}$$

where

$$\boldsymbol{H}(z) = (z^3\mathbf{I} + z^2\boldsymbol{A}_2 + z\boldsymbol{A}_1 + \boldsymbol{A}_0)^{-1}(z\boldsymbol{B}_1 + \boldsymbol{B}_0) \tag{28}$$

and the coefficient matrices are

$$\begin{aligned} \boldsymbol{A}_0 &= \boldsymbol{G}(\boldsymbol{K}_2\boldsymbol{G}^{-1}\boldsymbol{F} + \boldsymbol{K}_i - \boldsymbol{K}_1) \\ \boldsymbol{A}_1 &= \boldsymbol{F} + \boldsymbol{G}[\boldsymbol{K}_1 - \boldsymbol{K}_2\boldsymbol{G}^{-1}(\mathbf{I} + \boldsymbol{F})] \\ \boldsymbol{A}_2 &= \boldsymbol{G}\boldsymbol{K}_2\boldsymbol{G}^{-1} - \mathbf{I} - \boldsymbol{F} \\ \boldsymbol{B}_0 &= \boldsymbol{G}(\boldsymbol{K}_i - \boldsymbol{K}_t) \quad \boldsymbol{B}_1 = \boldsymbol{G}\boldsymbol{K}_t. \end{aligned} \tag{29}$$

It is to be noted that $\boldsymbol{B}_0$ depends on the other coefficient matrices, i.e., $\boldsymbol{B}_0 = \mathbf{I} + \boldsymbol{A}_2 + \boldsymbol{A}_1 + \boldsymbol{A}_0 - \boldsymbol{B}_1$, which also agrees with the steady-state condition $\boldsymbol{H}(1) = \mathbf{I}$. The gain matrices can be solved from (29) as

$$\begin{aligned} \boldsymbol{K}_t &= \hat{\boldsymbol{G}}^{-1}\boldsymbol{B}_{1\star} \quad \boldsymbol{K}_2 = \mathbf{I} + \hat{\boldsymbol{G}}^{-1}(\hat{\boldsymbol{F}} + \boldsymbol{A}_{2\star})\hat{\boldsymbol{G}} \\ \boldsymbol{K}_1 &= \boldsymbol{K}_2\hat{\boldsymbol{G}}^{-1}(\mathbf{I} + \hat{\boldsymbol{F}}) - \hat{\boldsymbol{G}}^{-1}(\hat{\boldsymbol{F}} - \boldsymbol{A}_{1\star}) \\ \boldsymbol{K}_i &= \boldsymbol{K}_1 - \boldsymbol{K}_2\hat{\boldsymbol{G}}^{-1}\hat{\boldsymbol{F}} + \hat{\boldsymbol{G}}^{-1}\boldsymbol{A}_{0\star}. \end{aligned} \tag{30}$$

Using these expressions, the poles and transmission zeros of (28) can be arbitrarily placed. The gains depend on the rotor speed via the matrices $\hat{\boldsymbol{F}}$ and $\hat{\boldsymbol{G}}$.

D. Selection of Coefficient Matrices

General control objectives for current controllers are the same as in the continuous-time case (see Section III-C). Hence, the nondiagonal elements of $\boldsymbol{H}(z)$ in (28) should be zero in order to avoid cross coupling of the axes, and the diagonal elements should be equal in order to achieve the same dynamics for both the axes. In the following, discrete-time variants of the two controller designs considered in Section III-C are given. Due to the time delay, $\boldsymbol{A}_{0\star} = \mathbf{O}$ is selected.

1) Internal Model Control Design: The discrete-time counterpart to the internal model control design in (13) is

$$\boldsymbol{A}_{1\star} = \beta^2\mathbf{I} \quad \boldsymbol{A}_{2\star} = -2\beta\mathbf{I} \quad \boldsymbol{B}_{1\star} = (1-\beta)\mathbf{I}. \tag{31}$$

TABLE I
DATA OF THE 6.7-kW SYRM

Rated values		
Phase voltage (peak value)	$\sqrt{2/3}$·370 V	1.00 p.u.
Current (peak value)	$\sqrt{2}$·15.5 A	1.00 p.u.
Frequency	105.8 Hz	1.00 p.u.
Speed	3175 r/min	1.00 p.u.
Motor parameters		
d-axis inductance L_d	45.6 mH	2.20 p.u.
q-axis inductance L_q	6.84 mH	0.33 p.u.
Stator resistance R_s	0.55 Ω	0.04 p.u.
PM flux ψ_f	0	0

The corresponding desirable closed-loop transfer function matrix is

$$\boldsymbol{H}_\star(z) = \frac{1-\beta}{z(z-\beta)}\mathbf{I} \tag{32}$$

where $\beta = e^{-\alpha T_s}$ is the exact mapping in the discrete domain of the intended real pole of the system. The diagonal matrix $\boldsymbol{H}_\star(z)$ consists of the delay and the first-order unity-gain low-pass filter. In digital control, the computational time delay z^{-1} cannot be avoided in practice. The same input parameters for the design are needed as in the continuous-time case ($\hat{R}_s$, $\hat{L}_d$, $\hat{L}_q$, and α).

2) Complex Vector Design: The discrete-time counterpart to the complex vector design in (16) is

$$\boldsymbol{A}_{1\star} = \beta^2\hat{\boldsymbol{F}} \quad \boldsymbol{A}_{2\star} = -\beta(\mathbf{I}+\hat{\boldsymbol{F}}) \quad \boldsymbol{B}_{1\star} = (1-\beta)\mathbf{I} \tag{33}$$

which also leads to reference tracking (32). The disturbance-rejection transfer function matrix is not diagonalized, but the open-loop poles are moved in an analogous manner to the continuous-time case. Furthermore, it can be seen that both (31) and (33) lead to deadbeat control if $\beta = 0$ is selected (or, equivalently, as α approaches infinity).

VI. RESULTS

In the following, discrete-time current control designs are evaluated by means of the robustness analysis, simulations, and experiments. The studied motor is a transverse-laminated 6.7-kW four-pole SyRM, whose data are given in Table I. Four variants of the complex vector design are considered:

- Design 1: approximation of the continuous-time design;
- Design 2: proposed design based on the approximate model with $\boldsymbol{\Psi} = \mathbf{I}$;
- Design 3: proposed design based on the approximate model with $\boldsymbol{\Psi} = \mathbf{I} + (T_s/2)\boldsymbol{F}_c$;
- Design 4: proposed design based on the exact model.

The performance of the internal model control design was also evaluated, but the results are not shown here for brevity.[3] Generally, the performance of the internal model control design is similar to the complex vector design, which, however, is more robust against parameter errors.

[3]Results for the internal model control design can be found in the conference version [26] of this paper.

A. Robustness Analysis

The robustness of the four current control designs against parameter errors is analyzed by calculating the poles of (28). The poles of (28) are the zeros of $\det(z^3\mathbf{I} + z^2\boldsymbol{A}_2 + z\boldsymbol{A}_1 + \boldsymbol{A}_0)$. The system is stable if all the poles are inside the unit circle. It is worth noticing that $\boldsymbol{F}$ and $\boldsymbol{G}$ are the exact system matrices calculated using the actual motor parameters, whereas the gains can be based on approximations and erroneous parameter estimates (depending on the control design under analysis). If the control design is based on the exact model and the motor parameters are perfectly known, the poles of (28) are equal to the desired closed-loop poles.

The controller gains have been calculated using the parameter estimates $\hat{L}_d = 2.20$ per unit (p.u.), $\hat{L}_q = 0.33$ p.u., and $\hat{R}_s = 0.04$ p.u. The desired bandwidth α is varied in a range from 0 to $2\pi \cdot 500$ rad/s. Fig. 2 shows the stability maps as a function of the desired bandwidth α and the ratio $L_q/\hat{L}_q$. The actual inductance L_q is varied in a range from 0 to $2.5\hat{L}_q$, whereas the other actual parameters perfectly match with their estimates. Fig. 2(a) and (b) shows the stability maps at zero speed when the sampling frequency is 1 and 2 kHz, respectively. It can be seen that Design 1 clearly has the smallest stable regions: the desired bandwidth α is limited to about $2\pi \cdot 75$ rad/s when the sampling frequency is 1 kHz and to about $2\pi \cdot 150$ rad/s when the sampling frequency is 2 kHz. The stable regions of Design 3 and Design 4 basically overlap with those of Design 2, i.e., there are no significant differences between Design 2 and Design 4. A comparison of Fig. 2(a) and (b) shows that increasing the sampling frequency from 1 to 2 kHz makes the stable regions larger in all the designs. It is to be noted that, if $L_q > \hat{L}_q$, the actual bandwidth becomes generally lower than the desired bandwidth α.

Fig. 2(c) and (d) shows the stability maps at the electrical angular speed $\omega_m = 2\pi \cdot 200$ rad/s when the sampling frequency is 1 and 2 kHz, respectively. The desired bandwidth α of Design 1 is limited to about $2\pi \cdot 20$ rad/s when the sampling frequency is 1 kHz and to about $2\pi \cdot 100$ rad/s when the sampling frequency is 2 kHz. The stable regions of Design 3 and Design 4 are comparatively large. A comparison of Fig. 2(a) and (b) shows that increasing the sampling frequency from 1 to 2 kHz significantly increases the stable regions of Design 1 and Design 2.

The robustness against erroneous $\hat{L}_d$ and $\hat{R}_s$ has been also analyzed. In the case of $\hat{L}_d$, the results are very similar to those in Fig. 2 and are not shown here. Design 2 to Design 4 are almost insensitive to errors in $\hat{R}_s$ in the whole speed range. As an example, Fig. 3 shows the stability maps as a function of the desired bandwidth α and the ratio $R_s/\hat{R}_s$. The actual resistance R_s is varied in a range from 0 to $2.5\hat{R}_s$, whereas other actual parameters perfectly match with their estimates. The speed is $\omega_m = 2\pi \cdot 200$ rad/s, and the sampling frequency is 1 kHz. It can be seen that the stable region of Design 2 is almost independent of the stator resistance error. Furthermore, the stable regions of Design 3 and Design 4 effectively cover the whole area.

The actual parameters were assumed to be constant (but erroneous) in this robustness analysis. In practice, the actual inductances may vary significantly (due to the magnetic saturation) even during one sampling period, which causes additional bandwidth limitations.

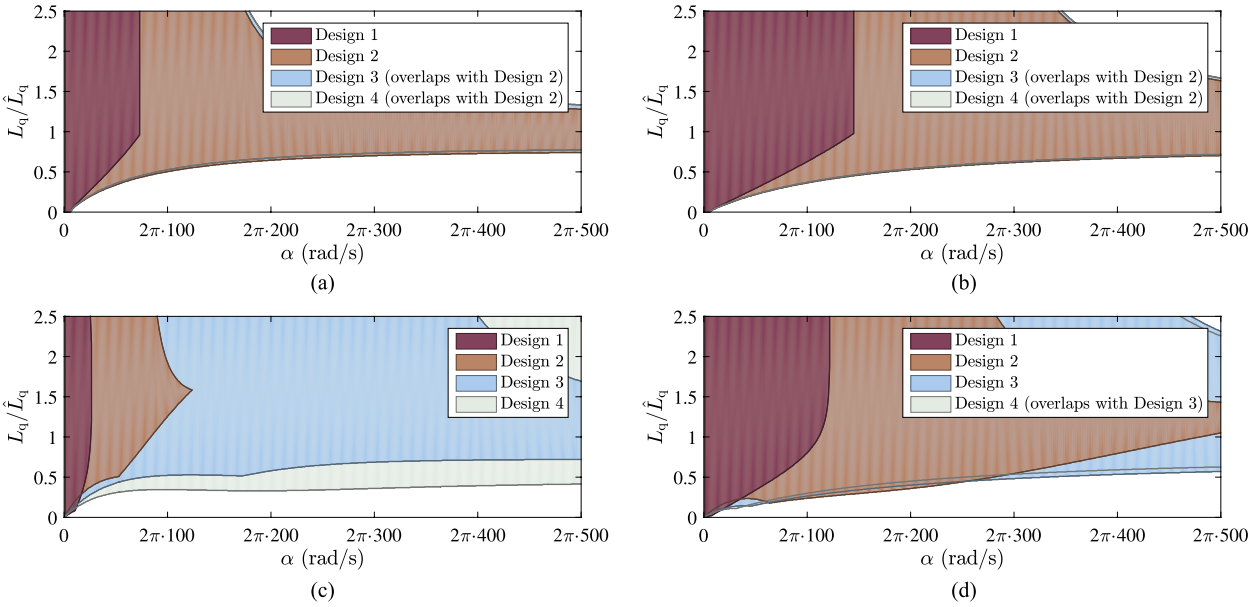

Fig. 2. Stability maps for the four different current control designs as a function of the desired bandwidth α and the ratio $L_q/\hat{L}_q$. (a) Electrical angular speed $\omega_m = 0$, the sampling frequency $f_s = 1$ kHz. (b) $\omega_m = 0$, $f_s = 2$ kHz. (c) $\omega_m = 2\pi \cdot 200$ rad/s, $f_s = 1$ kHz. (d) $\omega_m = 2\pi \cdot 200$ rad/s, $f_s = 2$ kHz.

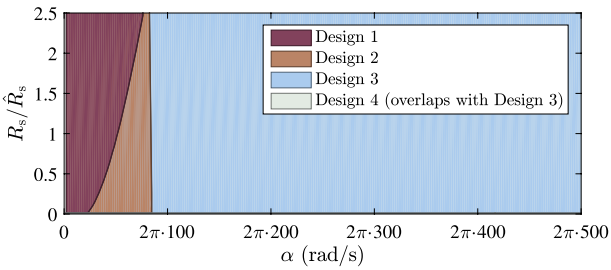

Fig. 3. Stability maps for the four different current control designs as a function of the desired bandwidth α and the ratio $R_s/\hat{R}_s$. The speed is $\omega_m = 2\pi \cdot 200$ rad/s, and the sampling frequency is $f_s = 1$ kHz.

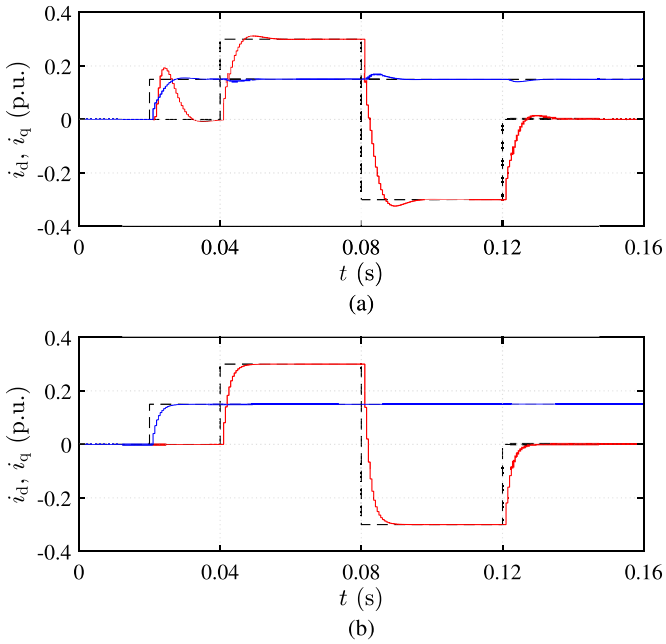

Fig. 4. Simulation results at the speed $\omega_m = 2\pi \cdot 200$ rad/s with the accurate parameter estimates. (a) Design 2. (b) Design 4. Sampled values of i_d (blue), i_q (red), and their references (black) are shown.

B. Simulation Results

Figs. 4 and 5 show the time-domain simulation results of the current waveforms. The electrical angular speed of the rotor is $\omega_m = 2\pi \cdot 200$ rad/s. The desired bandwidth is $\alpha = 2\pi \cdot 100$ rad/s, and the sampling frequency is 2 kHz. The current references $i_{d,\mathrm{ref}}$ and $i_{q,\mathrm{ref}}$ are changed stepwise: $i_{d,\mathrm{ref}}$ steps from 0 to 0.15 p.u. at $t = 0.02$ s; $i_{q,\mathrm{ref}}$ steps first from 0 to 0.3 p.u. at $t = 0.04$ s, then to -0.3 p.u. at $t = 0.08$ s, and finally back to 0 at $t = 0.12$ s. The sampled values of the current components i_d and i_q are shown (but the ripple between the sampling instants is fairly large at this low sampling frequencies; see [8]).

Fig. 4(a) and (b) shows the results for Design 2 and Design 4, respectively. The actual parameters perfectly match with their estimates. Significant cross coupling after $t = 0.02$ s and some overshoots appear in Fig. 4(a), whereas the results in Fig. 4(b) completely agree with the desired performance. The results for Design 1 and Design 3 are not shown for brevity: Design 1 is almost unstable in accordance with the stability map in Fig. 2(d), and the results for Design 3 are almost equal to those for Design 4 at this sampling frequency of 2 kHz. The performance of Design 3 starts to degrade at sampling frequencies roughly below 1.5 kHz, whereas Design 4 works perfectly at very low sampling frequencies (within the limits of the sampling theorem) in these ideal conditions. The numeric per-unit values of the gain matrices corresponding to Fig. 4 are given in Appendix B for comparison purposes.

Fig. 5 demonstrates the effects of parameter mismatches on the step responses in the case of Design 4. The actual inductance is $L_q = 0.5\hat{L}_q$ in Fig. 5(a), where some oscillations appear. These oscillations could be also anticipated based on Fig. 2(d), where the given operating condition is close to the

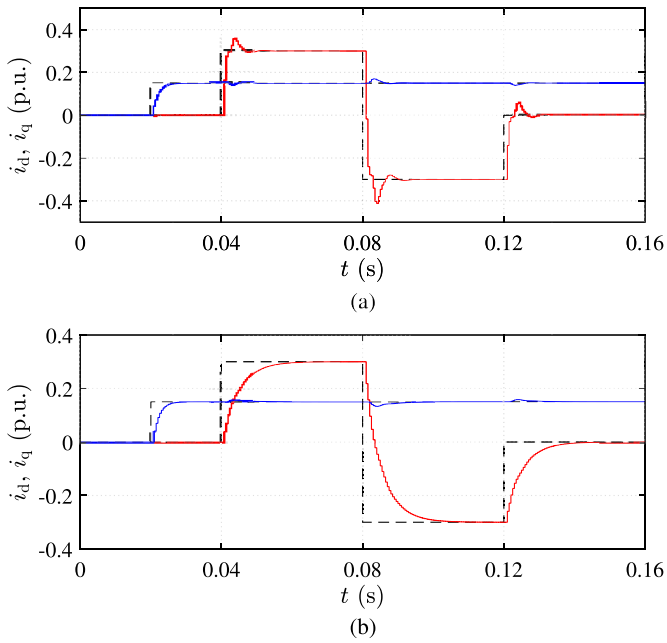

Fig. 5. Simulation results at the speed $\omega_m = 2\pi \cdot 200$ rad/s for Design 4. (a) $L_q = 0.5\hat{L}_q$. (b) $L_q = 2\hat{L}_q$.

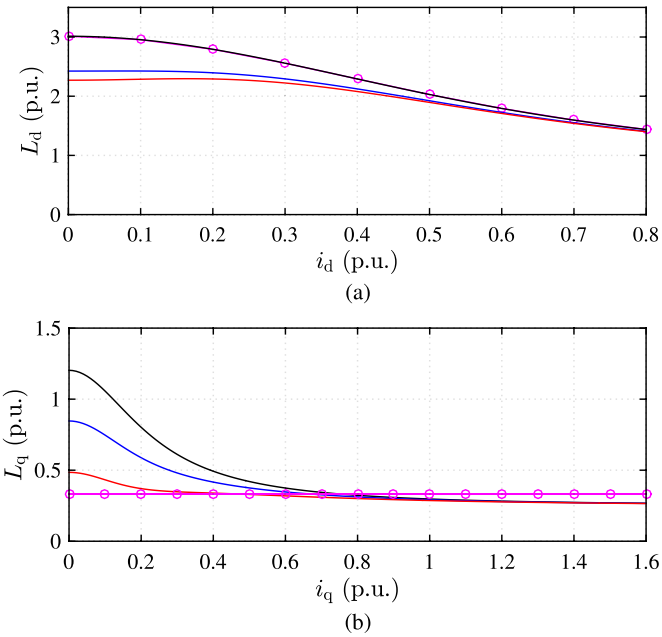

Fig. 6. Magnetic saturation characteristics of the 6.7-kW SyRM based on the measured inductances. (a) L_d as a function of i_d for $i_q = 0$ (black), 0.6 p.u. (blue), and 1.2 p.u. (red). (b) L_q as a function of i_q for $i_d = 0$ (black), 0.3 p.u. (blue), and 0.6 p.u. (red). The magenta curves with circle markers present the inductance estimates $\hat{L}_d(i_d)$ and $\hat{L}_q = 0.33$ p.u. used in the controller.

stability boundary. In Fig. 5(b), the actual inductance is $L_q = 2\hat{L}_q$. The step response is now well damped, but the actual bandwidth is less than the desired bandwidth.

C. Experimental Results

Design 3 and Design 4 were experimentally investigated using the 6.7-kW SyRM drive, but only the results for Design 4 are shown in the following for brevity. A servo induction machine was used as a loading machine in the speed-control mode. The controllers were implemented in a dSPACE DS1104 PPC/DSP board. The sampling is synchronized with the PWM. The sampling and switching frequencies are 2 kHz. The desired bandwidth is $\alpha = 2\pi \cdot 100$ rad/s.

The actual inductances of the SyRM depend significantly on the current components due to the magnetic saturation, as shown in Fig. 6 (see Appendix C). In the controller, however, a simple saturation model is applied. The d-axis inductance estimate depends only on i_d as

$$\hat{L}_d(i_d) = \frac{L_{d0} - L_{d\infty}}{1 + a_{d2} i_d^2 + a_{d4} i_d^4} + L_{d\infty} \tag{34}$$

where the parameters $L_{d0} = 3.01$ p.u., $L_{d\infty} = 0.89$ p.u., $a_{d2} = 2.79$ p.u., and $a_{d4} = 2.67$ p.u. correspond to the no-load condition. The constant value $\hat{L}_q = 0.33$ p.u. for the q-axis inductance estimate is used. The inductance estimates are also illustrated in Fig. 6.

Fig. 7 shows examples of the experimental results for Design 4. The current references are changed stepwise at zero speed in Fig. 7(a). It can be seen that the control response is close to the desired response despite the simple saturation model in the controller. Design 3 gave similar results, in accordance with the stability maps in Fig. 2(b).

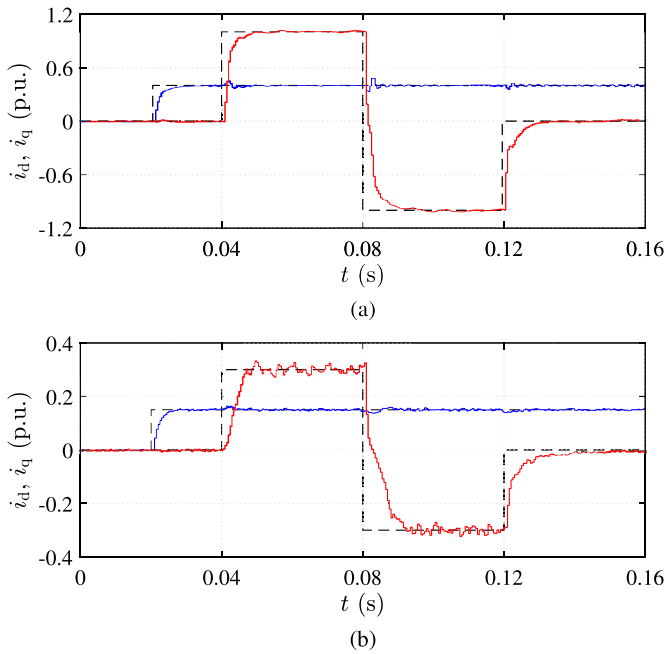

Fig. 7. Experimental results for Design 4. (a) $\omega_m = 0$. (b) $\omega_m = 2\pi \cdot 200$ rad/s.

Fig. 7(b) shows the current reference steps at the speed $\omega_m = 2\pi \cdot 200$ rad/s. The stator voltage is approximately zero until $t = 0.02$ s, but after the step in $i_{d,\mathrm{ref}}$, the voltage increases up to about 80% of the rated value. Despite this challenging transient condition, there is almost no cross coupling between the components of the stator current. The response of i_q is slightly slower than the desired response, particularly after

$t = 0.04$ s and after $t = 0.08$ s, where $|i_q|$ increases from the zero level. This skewing of the response can be understood based on the saturation characteristics shown in Fig. 6(b), where $L_q > 2\hat{L}_q$ at $i_q = 0$. At this sampling frequency of 2 kHz, the results for Design 3 were very similar to those for Design 4. The selection between Design 3 and Design 4 can be seen as a tradeoff between the computation time and the memory usage.

Lowering the sampling frequency down to 1 kHz caused a severe ripple in the current components at high speeds. Based on the time-domain simulations (with the saturation characteristics of the SyRM modeled), this ripple is induced by the combined effect of the nonlinear actual inductances and the very low sampling frequency. It might be possible to mitigate the ripple by improving the saturation model in the controller, but compensating for the effect of the differential inductances is not trivial [2], [12].

VII. Conclusion

An exact closed-form hold-equivalent discrete model of IPM and SyRM drives has been derived. The model can be applied to design, analysis, and implementation of controllers and observers. Furthermore, an analytical discrete-time pole-placement design method for a 2DOF PI current controller was proposed. The time delays are inherently taken into account in the design. The proposed design method is easy to apply: only the desired closed-loop bandwidth and three motor parameters are needed. The hold-equivalent model applied in the current control design can be either the exact model or a series expansion (where one more term than in the Euler method already gives good results). According to the results of eigenvalue analysis, simulations, and experiments, the proposed design improves the dynamic performance and robustness, particularly at high speeds, compared with the benchmark methods. The design method is directly applicable to SPM drives as well.

Appendix A
Derivation of the Exact Discrete-Time Model

A. Continuous-Time Model

In order to simplify the derivation of the exact discrete-time model, the stator-flux vector $\boldsymbol{\psi}_s$ is chosen as a state variable. The state-space representation corresponding to (3) is

$$\frac{d\boldsymbol{\psi}_s(t)}{dt} = \boldsymbol{A}\boldsymbol{\psi}_s(t) + \boldsymbol{B}\boldsymbol{u}_s(t) + \boldsymbol{b}\psi_f \tag{35a}$$

$$\boldsymbol{i}_s(t) = \boldsymbol{C}\boldsymbol{\psi}_s(t) + \boldsymbol{d}\psi_f \tag{35b}$$

where the system matrices are

$$\boldsymbol{A} = \begin{bmatrix} -R_s/L_d & \omega_m \\ -\omega_m & -R_s/L_q \end{bmatrix} \quad \boldsymbol{B} = \mathbf{I}, \quad \boldsymbol{b} = \begin{bmatrix} \frac{R_s}{L_d} \\ 0 \end{bmatrix}$$

$$\boldsymbol{C} = \begin{bmatrix} \frac{1}{L_d} & 0 \\ 0 & \frac{1}{L_q} \end{bmatrix} \quad \boldsymbol{d} = \begin{bmatrix} -1/L_d \\ 0 \end{bmatrix}. \tag{36}$$

These matrices are linked with the system matrices in (4) as

$$\boldsymbol{F}_c = \boldsymbol{C}\boldsymbol{A}\boldsymbol{C}^{-1} \quad \boldsymbol{G}_c = \boldsymbol{C} \quad \boldsymbol{g}_c = \boldsymbol{C}\boldsymbol{b} - \boldsymbol{F}_c\boldsymbol{d}. \tag{37}$$

B. Hold-Equivalent Discrete-Time Model

1) Assumptions: In the derivation of hold-equivalent discrete-time models, two different approaches to model the stator-voltage input have been used in the literature depending on whether the ZOH of the voltage input is assumed to be in rotor coordinates [8], [25] or in stator coordinates [7], [9]. An additional compensation for the delay due to the ZOH is needed in the first approach [25]. The latter approach is chosen here, since it inherently takes the ZOH delay properly into account.

Sampling of the stator currents is synchronized with the ZOH, and the switching cycle averaged quantities are considered. Under these assumptions, the actual stator voltage $\boldsymbol{u}_s^s(t)$ in stator coordinates is constant during $kT_s < t < (k+1)T_s$. The stator voltage input in (35a) can be expressed in stator coordinates, leading to

$$\frac{d\boldsymbol{\psi}_s(t)}{dt} = \boldsymbol{A}\boldsymbol{\psi}_s(t) + \boldsymbol{B}'(t)\boldsymbol{u}_s^s(t) + \boldsymbol{b}\psi_f \tag{38}$$

where the time-varying input matrix is

$$\boldsymbol{B}'(t) = e^{-\vartheta_m(t)\mathbf{J}}. \tag{39}$$

As quasi-constant ω_m is assumed, $\vartheta_m(t) = \vartheta_m(0) + \omega_m t$ holds. Furthermore, the motor parameters R_s, L_d, L_q, and ψ_f are assumed to be quasi-constant.

2) Structure and System Matrices: When the stator flux is used as the state variable, the discrete-time state-space representation is given by

$$\boldsymbol{\psi}_s(k+1) = \boldsymbol{\Phi}\boldsymbol{\psi}_s(k) + \boldsymbol{\Gamma}\boldsymbol{u}_s(k) + \boldsymbol{\gamma}\psi_f \tag{40a}$$

$$\boldsymbol{i}_s(k) = \boldsymbol{C}\boldsymbol{\psi}_s(k) + \boldsymbol{d}\psi_f \tag{40b}$$

where $\boldsymbol{\Phi}$, $\boldsymbol{\Gamma}$, and $\boldsymbol{\gamma}$ are the discrete-time system matrices. The discrete-time state matrix is

$$\boldsymbol{\Phi} = e^{\boldsymbol{A}T_s} = \begin{bmatrix} \phi_{11} & \phi_{12} \\ \phi_{21} & \phi_{22} \end{bmatrix}. \tag{41}$$

The input matrix $\boldsymbol{B}'(t)$ in (39) corresponding to the stator voltage is time variant. Hence, the discrete-time input matrix becomes

$$\boldsymbol{\Gamma} = \int_0^{T_s} e^{\boldsymbol{A}\tau}\boldsymbol{B}'(T_s - \tau)d\tau \cdot e^{\vartheta_m(0)\mathbf{J}} = \begin{bmatrix} \gamma_{11} & \gamma_{12} \\ \gamma_{21} & \gamma_{22} \end{bmatrix}. \tag{42}$$

The input matrix corresponding to the PM flux is

$$\boldsymbol{\gamma} = \int_0^{T_s} e^{\boldsymbol{A}\tau}d\tau \cdot \boldsymbol{b} = \begin{bmatrix} \gamma_1 \\ \gamma_2 \end{bmatrix}. \tag{43}$$

It is important to notice that $e^{x+y} = e^x e^y$ does not hold for matrix exponentials in general. If the stator current is used as a state variable, the system matrices become

$$\boldsymbol{F} = \boldsymbol{C}\boldsymbol{\Phi}\boldsymbol{C}^{-1} \quad \boldsymbol{G} = \boldsymbol{C}\boldsymbol{\Gamma} \quad \boldsymbol{g} = \boldsymbol{C}\boldsymbol{\gamma} + (\mathbf{I} - \boldsymbol{F})\boldsymbol{d}. \tag{44}$$

3) Closed-Form Expressions: The closed-form solutions for the elements of $\boldsymbol{\Phi}$ in (41) are

$$\begin{aligned}\phi_{11} &= e^{-\sigma T_s}\left[\cosh(\lambda T_s) - \delta\frac{\sinh(\lambda T_s)}{\lambda}\right]\\ \phi_{22} &= e^{-\sigma T_s}\left[\cosh(\lambda T_s) + \delta\frac{\sinh(\lambda T_s)}{\lambda}\right]\\ \phi_{21} &= -\phi_{12} = -\omega_m e^{-\sigma T_s}\frac{\sinh(\lambda T_s)}{\lambda}\end{aligned} \tag{45}$$

where $\lambda = \sqrt{\delta^2 - \omega_m^2}$ and[4]

$$\sigma = \frac{R_s}{2}\left(\frac{1}{L_d} + \frac{1}{L_q}\right) \quad \delta = \frac{R_s}{2}\left(\frac{1}{L_d} - \frac{1}{L_q}\right). \tag{46}$$

The closed-form solutions for the elements of $\boldsymbol{\Gamma}$ in (42) are

$$\begin{aligned}\gamma_{11} &= G\Big[g_{11}\cos(\omega_m T_s) - g_{12}\sin(\omega_m T_s) - g_{11}\phi_{11}\\ &\qquad + (\sigma+\delta)\omega_m^2(\phi_{11} - \phi_{22})\Big]\\ \gamma_{12} &= G\Big[g_{12}\cos(\omega_m T_s) + g_{11}\sin(\omega_m T_s) - g_{12}\phi_{11} + g_{22}\phi_{21}\Big]\\ \gamma_{21} &= G\Big[g_{21}\cos(\omega_m T_s) - g_{22}\sin(\omega_m T_s) - g_{21}\phi_{22} - g_{11}\phi_{21}\Big]\\ \gamma_{22} &= G\Big[g_{22}\cos(\omega_m T_s) + g_{21}\sin(\omega_m T_s) - g_{22}\phi_{22}\\ &\qquad + (\sigma-\delta)\omega_m^2(\phi_{22} - \phi_{11})\Big]\end{aligned} \tag{47}$$

where $G = 1/[(\sigma^2 - \delta^2)^2 + 4\sigma^2\omega_m^2]$, and

$$\begin{aligned}g_{11} &= (\sigma-\delta)^2(\sigma+\delta) + 4\sigma\omega_m^2 \quad g_{12} = 2(\sigma-\delta)\delta\omega_m\\ g_{21} &= 2(\sigma+\delta)\delta\omega_m \quad g_{22} = (\sigma+\delta)^2(\sigma-\delta) + 4\sigma\omega_m^2.\end{aligned} \tag{48}$$

The elements of $\boldsymbol{\gamma}$ in (43) are given by

$$\begin{aligned}\gamma_1 &= H\left[(\sigma-\delta)(1-\phi_{11}) - \omega_m\phi_{21}\right]\\ \gamma_2 &= H\left[-\sigma\phi_{21} + \omega_m\left(\frac{\phi_{11}+\phi_{22}}{2} - 1\right)\right]\end{aligned} \tag{49}$$

where $H = (\sigma+\delta)/[(\sigma+\delta)(\sigma-\delta) + \omega_m^2]$.

In the special case $L_d = L_q$ corresponding to the SPM, the system matrices $\boldsymbol{\Phi}$ and $\boldsymbol{\Gamma}$ reduce to

$$\boldsymbol{\Phi} = e^{-\sigma T_s}e^{-\omega_m T_s\mathbf{J}} \quad \boldsymbol{\Gamma} = \frac{1 - e^{-\sigma T_s}}{\sigma}e^{-\omega_m T_s\mathbf{J}} \tag{50}$$

where $\sigma = R_s/L_d$. These expressions are mathematically identical to those given in [7] and [9].

[4]If $\omega_m^2 > \delta^2$, then $\lambda = j\lambda_{\mathrm{im}} = j\sqrt{\omega_m^2 - \delta^2}$ is imaginary. All the matrix elements remain real since $\cosh(j\lambda_{\mathrm{im}}T_s) = \cos(\lambda_{\mathrm{im}}T_s)$, and $\sinh(j\lambda_{\mathrm{im}}T_s)/(j\lambda_{\mathrm{im}}) = \sin(\lambda_{\mathrm{im}}T_s)/\lambda_{\mathrm{im}}$ holds due to the properties of hyperbolic functions. Furthermore, for $\lambda = 0$, these functions reduce to $\cosh(\lambda T_s) = \sinh(\lambda T_s)/\lambda = 1$.

APPENDIX B
NUMERIC VALUES OF THE GAIN MATRICES

For comparison purposes, the numeric values of the gain matrices have been computed for Design 2 and Design 4. The conditions correspond to the simulations shown in Fig. 4: $T_s = 0.5$ ms (0.332 p.u.), $\alpha = 2\pi\cdot 100$ rad/s (0.945 p.u.), $\omega_m = 2\pi\cdot 200$ rad/s (1.89 p.u.), and the parameters in Table I are used. The per-unit values for Design 2 are

$$\boldsymbol{K}_t = \begin{bmatrix}1.444 & -0.157\\ 1.049 & 0.217\end{bmatrix} \quad \boldsymbol{K}_i = \begin{bmatrix}-0.086 & -0.146\\ 0.950 & -0.007\end{bmatrix}$$
$$\boldsymbol{K}_1 = \begin{bmatrix}4.152 & 0.021\\ -0.064 & 0.606\end{bmatrix} \quad \boldsymbol{K}_2 = \begin{bmatrix}0.534 & 0.174\\ -0.165 & 0.532\end{bmatrix}$$

and the per-unit values for Design 4 are

$$\boldsymbol{K}_t = \begin{bmatrix}1.446 & -0.160\\ 1.058 & 0.221\end{bmatrix} \quad \boldsymbol{K}_i = \begin{bmatrix}0.148 & -0.160\\ 1.053 & 0.029\end{bmatrix}$$
$$\boldsymbol{K}_1 = \begin{bmatrix}3.355 & -0.006\\ 0.059 & 0.496\end{bmatrix} \quad \boldsymbol{K}_2 = \begin{bmatrix}0.486 & 0.157\\ -0.153 & 0.480\end{bmatrix}.$$

It can be seen that only the gain matrix $\boldsymbol{K}_2$ is almost skew symmetric. Furthermore, the values of the matrix $\boldsymbol{K}_t$ are similar for Design 2 and Design 4, whereas there are clear differences in the case of other matrices.

APPENDIX C
MAGNETIC SATURATION

The saturation characteristics of the 6.7-kW SyRM are described by rational functions similar to those in [27]. Here, the reciprocity condition $\partial\psi_d/\partial i_q = \partial\psi_q/\partial i_d$ [28], [29] is taken into account in order to reduce the number of parameters from 16 to 11, leading to

$$L_d(i_d, i_q) = L_{\mathrm{dd}}(i_d) - L_{\mathrm{dq}}(i_d, i_q) \tag{51a}$$
$$L_q(i_d, i_q) = L_{\mathrm{qq}}(i_q) - L_{\mathrm{qd}}(i_d, i_q) \tag{51b}$$

where

$$L_{\mathrm{dd}}(i_d) = \frac{L_{d0} - L_{d\infty}}{1 + a_{d2}i_d^2 + a_{d4}i_d^4} + L_{d\infty} \tag{52a}$$
$$L_{\mathrm{qq}}(i_q) = \frac{L_{q0} - L_{q\infty}}{1 + a_{q2}i_q^2 + a_{q4}i_q^4} + L_{q\infty} \tag{52b}$$
$$L_{\mathrm{dq}}(i_d, i_q) = \frac{L_{\mathrm{dq}0}c_q i_q^2}{(1 + c_d i_d^2)^2(1 + c_q i_q^2)} \tag{52c}$$
$$L_{\mathrm{qd}}(i_d, i_q) = \frac{L_{\mathrm{dq}0}c_q i_d^2}{(1 + c_q i_q^2)^2(1 + c_d i_d^2)}. \tag{52d}$$

The parameter values were obtained by fitting the inductance functions (51) to the measured inductances as described in [30]. The fitted per-unit values are $L_{d0} = 3.01$, $L_{d\infty} = 0.89$, $a_{d2} = 2.79$, $a_{d4} = 2.67$, $L_{q0} = 1.20$, $L_{q\infty} = 0.25$, $a_{q2} = 18.06$, $a_{q4} = 0$, $L_{\mathrm{dq}0} = 0.81$, $c_d = 5.44$, and $c_q = 7.25$. The inductance functions are illustrated in Fig. 6.

ACKNOWLEDGMENT

The authors would like to thank D. Koslopp for preliminary analyses of discrete models.

REFERENCES

[1] T. M. Rowan and R. J. Kerkman, "A new synchronous current regulator and an analysis of current-regulated PWM inverters," *IEEE Trans. Ind. Appl.*, vol. IA-22, no. 4, pp. 678–690, Jul./Aug. 1986.

[2] L. Springob and J. Holtz, "High-bandwidth current control for torque-ripple compensation in PM synchronous machines," *IEEE Trans. Ind. Electron.*, vol. 45, no. 5, pp. 713–721, Oct. 1998.

[3] L. Harnefors and H.-P. Nee, "Model-based current control of ac machines using the internal model control method," *IEEE Trans. Ind. Appl.*, vol. 34, no. 1, pp. 133–141, Jan./Feb. 1998.

[4] F. Briz del Blanco, M. W. Degner, and R. D. Lorenz, "Dynamic analysis of current regulators for ac motors using complex vectors," *IEEE Trans. Ind. Appl.*, vol. 35, no. 6, pp. 1424–1432, Nov./Dec. 1999.

[5] F. Briz, M. W. Degner, and R. D. Lorenz, "Analysis and design of current regulators using complex vectors," *IEEE Trans. Ind. Appl.*, vol. 36, no. 3, pp. 817–825, May/Jun. 2000.

[6] H. Kim and R. D. Lorenz, "Improved current regulators for IPM machine drives using on-line parameter estimation," in *Conf. Rec. IEEE IAS Annu. Meeting*, Pittsburgh, PA, USA, Oct. 2002, vol. 1, pp. 86–91.

[7] K.-K. Huh and R. D. Lorenz, "Discrete-time domain modeling and design for ac machine current regulation," in *Conf. Rec. IEEE IAS Annu. Meeting*, New Orleans, LA, USA, Sep. 2007, pp. 2066–2073.

[8] J.-S. Yim, S.-K. Sul, B.-H. Bae, N. R. Patel, and S. Hiti, "Modified current control schemes for high-performance permanent-magnet ac drives with low sampling to operating frequency ratio," *IEEE Trans. Ind. Appl.*, vol. 45, no. 2, pp. 763–771, Mar./Apr. 2009.

[9] H. Kim, M. W. Degner, J. M. Guerrero, F. Briz, and R. D. Lorenz, "Discrete-time current regulator design for ac machine drives," *IEEE Trans. Ind. Appl.*, vol. 46, no. 4, pp. 1425–1435, Jul./Aug. 2010.

[10] W. Peters, T. Huber, and J. Böocker, "Control realization for an interior permanent magnet synchronous motor (IPMSM) in automotive drive trains," in *Proc. PCIM*, Nuremberg, Germany, May 2011, vol. 1, pp. 98–103.

[11] O. Wallmark, S. Lundberg, and M. Bongiorno, "Input admittance expressions for field-oriented controlled salient PMSM drives," *IEEE Trans. Power Electron.*, vol. 27, no. 3, pp. 1514–1520, Mar. 2012.

[12] W. Peters and J. Bccker, "Discrete-time design of adaptive current controller for interior permanent magnet synchronous motors (IPMSM) with high magnetic saturation," in *Proc. IEEE IECON*, Vienna, Austria, Nov. 2013, pp. 6608–6613.

[13] A. Altomare, A. Guagnano, F. Cupertino, and D. Naso, "Discrete-time control of high speed salient machines," in *Proc. IEEE ECCE*, Pittsburgh, PA, USA, Sep. 2014, pp. 3528–3534.

[14] L. Harnefors, "Design and analysis of general rotor-flux-oriented vector control systems," *IEEE Trans. Ind. Electron.*, vol. 48, no. 2, pp. 383–390, Apr. 2001.

[15] J. Holtz *et al.*, "Design of fast and robust current regulators for high-power drives based on complex state variables," *IEEE Trans. Ind. Appl.*, vol. 40, no. 5, pp. 1388–1397, Sep./Oct. 2004.

[16] L. Harnefors, "Modeling of three-phase dynamic systems using complex transfer functions and transfer matrices," *IEEE Trans. Ind. Electron.*, vol. 54, no. 4, pp. 2239–2248, Aug. 2007.

[17] B. D. O. Anderson and D. G. Luenberger, "Design of multivariable feedback systems," *Proc. Inst. Elect. Eng.*, vol. 114, no. 3, pp. 395–399, Mar. 1967.

[18] J.-C. Alacoque, "Discrete-time modelling—Flux and torque deadbeat control for induction machine," in *Proc. EPE-PEMC*, Portorož, Slovenia, Aug./Sep. 2006, pp. 1099–1104.

[19] G. F. Franklin, J. D. Powell, and M. Workman, *Digital Control of Dynamic Systems*, 3rd ed. Menlo Park, CA, USA: Addison-Wesley, 1997.

[20] L. S. Shieh and Y. T. Tsay, "Transformations of a class of multivariable control systems to block companion forms," *IEEE Trans. Autom. Control*, vol. AC-27, no. 1, pp. 199–203, Feb. 1982.

[21] L. S. Shieh, Y. T. Tsay, and R. E. Yates, "State-feedback decomposition of multivariable systems via block-pole placement," *IEEE Trans. Autom. Control*, vol. AC-28, no. 8, pp. 850–852, Aug. 1983.

[22] J. S. Lee, C.-H. Choi, J.-K. Seok, and R. D. Lorenz, "Deadbeat-direct torque and flux control of interior permanent magnet synchronous machines with discrete time stator current and stator flux linkage observer," *IEEE Trans. Ind. Appl.*, vol. 47, no. 4, pp. 1749–1758, Jul./Aug. 2011.

[23] T. Geyer, "Model predictive direct torque control: Derivation and analysis of the state-feedback control law," *IEEE Trans. Ind. Appl.*, vol. 49, no. 5, pp. 2146–2157, Sep./Oct. 2013.

[24] L. Harnefors, K. Pietilöainen, and L. Gertmar, "Torque-maximizing field-weakening control: Design, analysis, and parameter selection," *IEEE Trans. Ind. Electron.*, vol. 48, no. 1, pp. 161–168, Feb. 2001.

[25] B.-H. Bae and S.-K. Sul, "A compensation method for time delay of full-digital synchronous frame current regulator of PWM ac drives," *IEEE Trans. Ind. Appl.*, vol. 39, no. 3, pp. 802–810, May/Jun. 2003.

[26] M. Hinkkanen, Z. Qu, H. A. A. Awan, T. Tuovinen, and F. Briz, "Current control for IPMSM drives: Direct discrete-time pole-placement design," in *Proc. IEEE WEMDCD*, Turin, Italy, Mar. 2015, pp. 156–164.

[27] S. Yamamoto, T. Ara, and K. Matsuse, "A method to calculate transient characteristics of synchronous reluctance motors considering iron loss and cross-magnetic saturation," *IEEE Trans. Ind. Appl.*, vol. 43, no. 1, pp. 47–56, Jan./Feb. 2007.

[28] J. A. Melkebeek and J. L. Willems, "Reciprocity relations for the mutual inductances between orthogonal axis windings in saturated salient-pole machines," *IEEE Trans. Ind. Appl.*, vol. 26, no. 1, pp. 107–114, Jan./Feb. 1990.

[29] A. Vagati, M. Pastorelli, F. Scapino, and G. Franceschini, "Impact of cross saturation in synchronous reluctance motors of the transverse-laminated type," *IEEE Trans. Ind. Appl.*, vol. 36, no. 4, pp. 1039–1046, Jul./Aug. 2000.

[30] Z. Qu, T. Tuovinen, and M. Hinkkanen, "Inclusion of magnetic saturation in dynamic models of synchronous reluctance motors," in *Proc. ICEM*, Marseille, France, Sep. 2012, pp. 994–1000.

Marko Hinkkanen (M'06–SM'13) received the M.Sc.(Eng.) and D.Sc.(Tech.) degrees from Helsinki University of Technology, Espoo, Finland, in 2000 and 2004, respectively.

He is currently an Assistant Professor with Aalto the School of Electrical Engineering, Aalto University, Espoo. His research interests include control engineering, electric drives, and power converters.

Hafiz Asad Ali Awan received the B.Sc. degree in electrical engineering from the University of Engineering and Technology, Lahore, Pakistan, in 2012 and the M.Sc.(Tech.) degree in electrical engineering from Aalto University, Espoo, Finland, in 2015. He is currently working toward the D.Sc.(Tech.) degree at Aalto University.

His main research interest is the control of electric drives.

Zengcai Qu received the B.Sc. degree in electrical engineering and automation from Shanghai Jiao Tong University, Shanghai, China, in 2007, the M.Sc.(Eng.) degree in space science and technology jointly from Lulea University of Technology, Kiruna, Sweden, and Helsinki University of Technology, Espoo, Finland, in 2009, and the D.Sc.(Tech.) degree from Aalto University, Espoo, in 2015.

He is currently with ABB Oy Drives, Helsinki, Finland. His research interests are power electronics and electric drives.

Toni Tuovinen received the M.Sc. degree from the University of Helsinki, Helsinki, Finland, in 2005, the M.Sc.(Eng.) degree from Helsinki University of Technology, Espoo, Finland, in 2009, and the D.Sc.(Tech.) degree from Aalto University, Espoo, in 2014.

He is currently a Senior Design Engineer with ABB Oy Drives, Helsinki. His main research interests include the control of electric drives.

Fernando Briz (A'96–M'99–SM'06) received the M.S. and Ph.D. degrees from the University of Oviedo, Gijón, Spain, in 1990 and 1996, respectively.

From June 1996 to March 1997, he was a Visiting Researcher with the University of Wisconsin–Madison, Madison, WI, USA. He is currently a Full Professor with the Department of Electrical, Electronic, Computer and Systems Engineering, University of Oviedo. His current research interests include control systems, power converters and ac drives, machine diagnostics, and digital signal processing.

Dr. Briz is currently the Program Chair and an Associate Editor of the Industrial Drives Committee of the IEEE Industry Applications Society Industrial Power Conversion Systems Department. He was a recipient of the 2005 IEEE TRANSACTIONS ON INDUSTRY APPLICATIONS Third Place Prize Paper Award and six IEEE Industry Applications Society Conference and IEEE Energy Conversion Congress and Exposition Prize Paper Awards.